PCCP

ROYAL SOCIETY OF CHEMISTRY

PAPER

View Article Online
View Journal | View Issue

Cite this: *Phys. Chem. Chem. Phys.*, 2025, **27**, 14613

Theoretical design of higher performance catalysts for ethylene polymerization based on nickel–α-diimine†

Pavee Apilardmongkol,[a] Manussada Ratanasak,*[b] Tatiya Chokbunpiam,[c] Fadjar Mulya,[d] Wilasinee Santiwarodom,[a] Thanawit Kuamit,[a] Yasuteru Shigeta,[b] Jun-ya Hasegawa[e] and Vudhichai Parasuk*[a]

Received 7th April 2025,
Accepted 20th June 2025

DOI: 10.1039/d5cp01320h

rsc.li/pccp

In this study, we investigated the reaction mechanism of Ni–α-diimine catalysts for ethylene (ET) polymerization using DFT calculations, focusing on structural and electronic factors that govern catalyst performance. Being the most active catalyst, Ni–Me was kept as a reference for analyzing pre-catalyst stability and reaction mechanisms. The first ET insertion, exhibiting the highest coordination free energy (G_{c1}) and activation free energy ($\Delta G_1^{\ddagger}$), is the rate-determining step. A comparative analysis of M–α-diimine catalysts with different transition metals (M = Mn(II), Fe(II), Co(II), Ni(II), Cu(II), Zn(II), Ru(II), Rh(II), Pd(II), Ag(I), Cd(II)) revealed three distinct clusters. The cluster which contains (Ni(II), Ru(II), Mn(II), Rh(II), and Pd(II)) has moderate binding strength (G_{c1} between −20 and −10 kcal mol^{-1}) and a reasonable activation barrier ($\Delta G_1^{\ddagger}$ between 10 and 15 kcal mol^{-1}), making it the most promising group for further study. With these criteria, Mn(II), Rh(II), Pd(II), Fe(II), and Ru(II) were identified as strong candidates for further catalyst development. Additionally, the bond distances and the percent buried volume (%V_{Bur}) were identified as key steric factors significantly influencing catalyst performance. These insights provide a rational framework for designing next-generation M–α-diimine catalysts with enhanced activity in ethylene polymerization.

Introduction

Polyethylene (PE) is a lightweight, durable thermoplastic with a variable crystalline structure. As the largest class of plastics, the PE market experiences a steady 5–6% annual growth due to its versatile physical and mechanical properties, non-toxic nature, energy-efficient and economically attractive production, and the availability of low-cost raw materials.[1] In the industrial sector, PE is traditionally produced through catalyzed olefin polymerization with heterogeneous Ziegler–Natta catalysts, which have been used since the 1950s.[2] Nevertheless, these catalysts have limitations arising from the presence of multiple active sites in their structures. Consequently, there is a growing interest in developing single site metallocene catalysts within the polyolefin industry.

Numerous studies[3–6] have shown that neutral phenoxy-imine nickel catalysts or unsymmetrical α-diimine Ni(II) and Pd(II) catalysts exhibit high activity for ethylene polymerization. The α-diimine nickel dihalide complexes (LNiX_2: L = α-diimine ligand, X = halide, *e.g.*, Cl, Br), which can be easily prepared through the complexation of α-diimine ligands and nickel precursors, have garnered considerable attention due to their excellent catalytic performances.[7] The α-diimine nickel catalysts can polymerize conjugated monomers through catalyst-transfer polymerization and are well-known for catalyzing olefin polymerization *via* the coordination-insertion mechanism.[8]

The Brookhart group[9] significantly advanced the field by developing a series of α-diimine nickel/palladium complexes that catalyze ethylene (ET) polymerization, producing high molecular weight polyethylene. This breakthrough paved the way for late transition metal catalysts to significantly contribute to ET and olefin polymerization processes. Subsequently, researchers have developed a variety of influential late transition metal catalysts for ET polymerization.[9–11] The α-diimine

[a] *Center of Excellence in Computational Chemistry, Department of Chemistry, Faculty of Science, Chulalongkorn University, Pathumwan, Bangkok 10330, Thailand. E-mail: Vudhichai.P@chula.ac.th*
[b] *Center for Computational Sciences, University of Tsukuba, 1-1-1 Tennodai, Tsukuba, Ibaraki 305-8577, Japan. E-mail: manussada@ccs.tsukuba.ac.jp*
[c] *Department of Chemistry, Faculty of Science, Ramkhamhaeng University, Bangkok 10240, Thailand*
[d] *Nanotechnology Engineering Program, Faculty of Advanced Technology and Multidiscipline, Universitas Airlangga, Surabaya 60115, Indonesia*
[e] *Institute for Catalysis, Hokkaido University, Kita21, Nishi10, Kita-ku, Sapporo, Hokkaido 001-0021, Japan*

† Electronic supplementary information (ESI) available. See DOI: https://doi.org/10.1039/d5cp01320h

nickel/palladium catalyst, known for its unique chain walking mechanism, is notable for its ability to produce branched polyethylene materials. The density of branches can be easily adjusted by altering the polymerization temperature and pressure, providing versatile potential applications.[12] Nickel-based catalysts are more valuable for industrial applications when compared to palladium, primarily because of their cost advantages.[13]

Zhu *et al.*[14] conducted complementary experimental and computational studies on the thermal stability of α-diimine nickel complexes. To elucidate the mechanism governing the thermal stability of these catalysts, the decomposition energies of two α-diimine nickel complexes were calculated using first-principles calculations based on density functional theory (DFT). The results offer valuable insights and contribute significantly to the advancement of thermally stable catalysts for industrial applications. Wang and Chen[15] summarized some recent advances in α-diimine ligand modifications. The modification of Brookhart-type α-diimine nickel and palladium catalysts can be categorized into three aspects: (i) modifications of *N*-aryl substituents, (ii) modifications of ligand backbone structures, and (iii) utilization of di-nucleating ligands.

The backbone part of the α-diimine ligands plays a crucial role affecting catalyst stability, activity, and polymer properties. Several M–α-diimine with different backbones have been reported, for example, pyrenyl backbone[16] (Fig. 1A), naphthyl backbone[14] (Fig. 1B), dibenzobarrelene backbone[17] (Fig. 1C), acenaphthene backbone[18] (Fig. 1D), and thiophene backbone[19] (Fig. 1E). Experimental activities[20–26] of Ni(II) and Pd(II) catalysts with different backbones was summarized in Table S1 of the ESI.† The thiophene backbone (E) appears to provide better activity than other types of backbone. This is probably due to the reduction of the rigidity and steric hindrance surrounding the backbone moieties, along with increase in the flexibility of the *N*-aryl moieties around the metal center. Therefore, the thiophene backbone was selected in this present study.

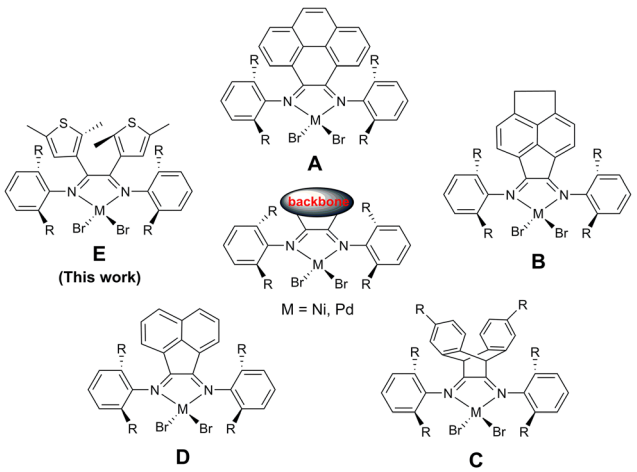

Fig. 1 Examples of M–α-diimine with different backbones. (A) Pyrenyl backbone (B) naphthyl backbone (C) dibenzobarrelene backbone (D) acenaphthene backbone, and (E) thiophene backbone.

Liao *et al.*[19] investigated the influence of a thiophenyl-based twisted backbone on the properties of α-diimine nickel catalysts in ET polymerization. They reported the experimental activities of α-diimine-type nickel catalysts and explored the impact of backbone structures. Specifically, nickel complexes bearing 2,5-dimethyl-thien-3-yl and 2-methyl-5-phenylthien-3-yl backbone structures exhibit much higher catalytic activity and thermal stability, up to 80 °C, in ET polymerization. These new nickel complexes generated polymer products with significantly higher molecular weight, lower branching density, and higher melting points. The bulky substituents at the ligand backbone influenced the *N*-aryl moieties, increasing steric bulkiness around the metal center. This backbone strategy holds promise for future studies in other catalytic reactions.

Zheng *et al.*[27] synthesized α-diimine di-bromo nickel complexes. Square-planar geometries and Ni–phenyl interactions in both solid and solution phases were identified using single-crystal X-ray diffraction analysis, NMR analysis, and DFT calculations. They found that bulky α-diimine nickel complexes enhance activity and thermal stability, resulting in the production of unexpectedly lightly branched PEs. Furthermore, weak attractive interactions between nickel and phenyl groups lead to a decrease in the branching density of PE during ET polymerization. Yan *et al.*[28] explored the polymerization mechanisms of ET catalyzed by two cationic nickel catalysts through DFT calculations. Their findings indicated that the stronger interaction can be explained by the more positive natural bond orbital (NBO) charge of the metal center and the smaller energy gap between the highest occupied molecular orbital (HOMO) of ET and the lowest unoccupied molecular orbital (LUMO) of the active intermediate. Additionally, a combination of multivariate linear regression (MLR) and DFT calculations has been employed to analyze and verify the factors influencing the ET polymerization activity of catalysts.

The most common mechanism for olefin polymerization was proposed by Cossee–Arlman[29] and Brookhart and Green.[30] The proposed mechanism of ET polymerization by α-diimine nickel catalyst is depicted in Scheme 1. The chain walking mechanism was represented similarly to previous studies.[31–33] This process can shift the β-elimination reaction from the polymer chain end to internal positions, resulting in the formation of branched polyethylene. The structure includes an MAO counteranion and explicit solvents. Typically, the counteranion influences catalytic activity by serving as an activator for the metal center, enhancing the catalyst's efficiency in ethylene polymerization. In this mechanism, ET is first inserted into the vacant site of the transition metal (M), forming the π-complex reactant (R_1). Then, a four-membered ring transition state (TS_1) is produced, resulting in the product (P_1) through an exothermic process.[8,34,35] Subsequently, the structure rearranges to form the active complex which is then ready for the next ET insertion. The reaction continues with a new ET monomer being inserted into the transition metal, similar to the first insertion. The reaction proceeds along with the π-complex reactant (R_2), then the four-membered ring transition state (TS_2), the product (P_2), the π-complex reactant

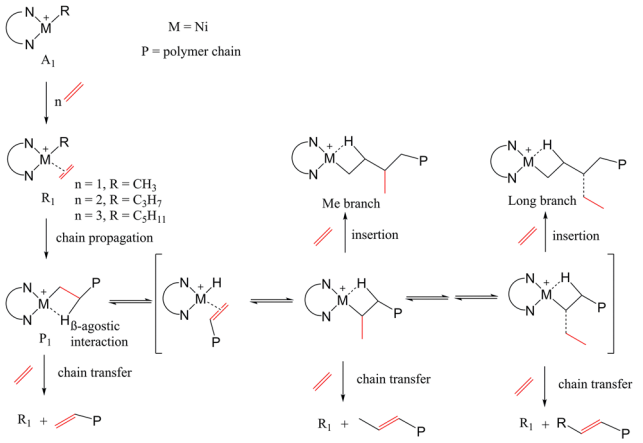

Scheme 1 Proposed reaction mechanism of ethylene polymerization by Ni–α-diimine catalysts.

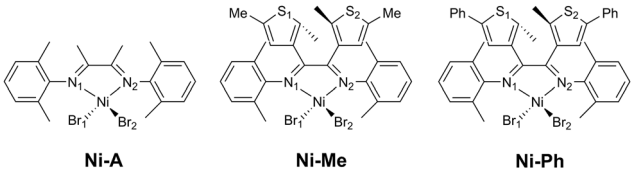

Fig. 2 The pre-catalyst models of α-diimine catalysts.

(R_3), then the four-membered ring transition state (TS_3), and finally, the product (P_3). The intermediate complex was utilized to link the first and second insertions (I_{12}) as well as the second and third insertions (I_{23}). The chain-walking mechanism exhibits in the β-agostic species, which can be formed either after olefin insertion from the metal-(alkyl)olefin resting state *via* β-H elimination, olefin rotation, and reinsertion.[8,22,36,37] These mechanistic insights into the effects of metal centers effectively explain the distinct ethylene polymerization behaviors, offering valuable guidelines for designing polymerization catalysts with different metal centers.[38]

In conventional olefin polymerizations, electrophilic early transition metal (groups 3 and 4)-based catalysts have considerable limitations despite their remarkable effectiveness.[39] Late-transition-metal α-diimine complexes, particularly those of Ni(II) and Pd(II), have attracted significant attention as catalysts for ET polymerization due to their unique ability and high activities. Since their introduction by Brookhart and co-workers,[7–9] these catalysts have become a benchmark system for tuning polymer microstructure *via* metal design or ligand design. Despite the widespread of Ni(II) and Pd(II) systems, efforts to explore alternative metal centers remain limited, largely due to uncertainties about their electronic properties, geometries, and potential catalytic activity. Although Ni(II) and Pd(II) α-diimine complexes have been the subject of numerous experimental investigations, there are still few systematic theoretical comparisons across the periodic table.

In this work, we investigated the reaction mechanism of ET polymerization catalyzed by α-diimine nickel complexes using the DFT calculations. The α-diimine nickel catalyst bearing 2,5-dimethyl-thien-3-yl (Ni–Me, as shown in Fig. 2) was selected for this study due to its superior catalytic activity and thermal stability. The structural models of the α-diimine nickel catalysts were constructed based on X-ray crystallographic data obtained from prior experiments.[19] Subsequently, we analyzed the reaction mechanism of Ni–α-diimine-catalyzed ET polymerization by examining the relative Gibbs free energy profile, with particular attention to the structural and electronic features at the reaction's rate-determining step. We calculated the coordination free energy (G_c), activation free energy ($\Delta G^{\ddagger}$), and reaction free energy (ΔG_r) to evaluate the binding capability and the overall reaction process. We further performed a comprehensive DFT-based screening of late transition metal α-diimine complexes (M = Mn(II), Fe(II), Co(II), Ni(II), Cu(II), Zn(II), Ru(II), Rh(II), Pd(II), Ag(I), and Cd(II)), evaluating their potential as ethylene polymerization catalysts using physical properties such as %buried volume ($\%V_{Bur}$) and metal charge (q_M). Unlike previous work,[15] which typically focused on specific metals or ligand families, we investigate a broad range of metals while holding the ligand constant to isolate the effect of the metal center. We identify not only established catalytic candidates (*e.g.*, Ni(II), Pd(II)) but also potentially overlooked metals with promising energy criteria. This work aims to enhance the understanding of the reaction mechanism of ET polymerization and offers valuable insights for designing and developing catalysts in this field. The findings can contribute to reducing the cost of plastic production, improving catalytic efficiency, and advancing the industrial application of M–α-diimine catalysts.

Computational details

Catalyst models

Since the experimental activities of α-diimine-type nickel catalysts have been reported, the structures of α-diimine-type nickel catalysts based on the X-ray structures were obtained.[19] The three models chosen for this study are (1) the Brookhart type α-diimine nickel catalyst (Ni–A), (2) α-diimine nickel catalyst bearing 2,5-dimethyl-thien-3-yl (Ni–Me), and (3) α-diimine nickel catalyst bearing 2-methyl-5-phenylthien-3-yl (Ni–Ph). The pre-catalyst models of Ni–A, Ni–Me, and Ni–Ph are displayed in Fig. 1. While Ni–A represents the simplest Ni–α-diimine, originally reported by the Brookhart group, Ni–Me and Ni–Ph increase the steric bulkiness of the backbone moieties by incorporating thiophene groups. The substituents at the second and fifth positions of the thiophene moiety can influence both the axial metal center and the *N*-aryl groups. Among them, Ni–Me demonstrates significantly higher catalytic activity and thermal stability.[19]

Based on the proposed reaction mechanism depicted in Scheme 1. The coordination free energy (G_{cx}), activation free energy ($\Delta G_x^{\ddagger}$) and reaction free energy (ΔG_{rx}) were calculated by following equations:

$$G_{cx} = G_{Rx} - (G_{Ax} + G_{ET}) \quad (1)$$

$$\Delta G_x^{\ddagger} = G_{TSx} - G_{Rx} \quad (2)$$

$$\Delta G_{rx} = G_{Px} - G_{Rx} \quad (3)$$

where G_{Rx}, G_A, G_{TSx}, and G_{Px} are the Gibbs free energy of π-complex reactant (R), active-catalyst (A), transition-state (TS), and product (P) for the ET insertion, respectively. The subscript x = 1, 2, and 3 are referred to as the first, second, and third ET insertion, respectively.

DFT calculations

All the calculations were carried out using the Gaussian16 (Rev.C.01) program.[40] DFT calculations were performed by using the ωB97XD functional[41,42] with 6-31G(d) basis set[43] for non-metal atoms and with the Stuttgart/Dresden effective core potential (SDD)[44,45] and basis set for transition metals. The comparison of bond lengths, bond angles, and torsion obtained from different theoretical methods were given in Table S2 of the ESI.† The Gibbs free energies at 298 K and 1 atm were used to elucidate the free energy profile. All local energy minimum structures and transition state structures were confirmed by zero and one imaginary frequency, respectively. The progress of π-complex reactant to TS to product was verified by intrinsic reaction coordinate (IRC) calculations. Energies of structures were determined under gas phase conditions. For the calculations, the standard self-consistent energy convergence is 1.0×10^{-6} Hartree. The standard maximum displacement and maximum force convergence for the calculations are 1.8×10^{-3} Å and 4.5×10^{-4} Hartree Bohr^{-1}, respectively. Since the most stable spin state was implemented for calculations of each metal complex. Thus, the singlet spin state was assigned to Ni(II), Fe(II), Zn(II), Ru(II), Pd(II), Ag(I) and Cd(II), whereas a doublet spin state was used for Cu(II) and Rh(II), and a quartet spin state was applied to Mn(II) and Co(II). The natural population analysis (NPA)[46,47] was performed for the natural atomic charges (NBO) with Gaussian NBO Version 3.1. We assessed the solvent effect with the implicit SMD solvation model with toluene as a solvent (E_{ps} = 2.3741). The results of the G_{cx}, $\Delta G_x^{\ddagger}$, and ΔG_{rx} in the gas phase and the toluene solvent are given in Table S3 of the ESI.†

Results and discussion

Numerous studies have been devoted to the impact of the α-diimine backbone structure on the catalyst's performance and polymer properties.[48–50] Liao *et al.*[19] reported that the Ni–Me catalyst displayed the highest experimental activities at 20 °C followed by Ni–Ph, and Ni–A. To elucidate the structure dependence on catalytic activities, topographic steric maps of Ni–A, Ni–Me, and Ni–Ph were produced using SambVca2.1 program[51] to analyze the effect of steric hindrance in terms of the buried volume (%V_{Bur}).[52] Moreover, the structural comparison of Ni–A, Ni–Me, and Ni–Ph is shown in Fig. S1 of the ESI.†

In this catalytic reaction, the steric hindrance effect should be related to the buried volume of the nickel center. The heightened steric hindrance impedes the process of chain walking and reduces the density of branching of the product.[13] Fig. 3 shows the topographic steric maps of Ni–A, Ni–Me, and Ni–Ph of the pre-catalyst and active complexes. For the pre-catalyst complex, we found that the trend of %V_{Bur} is Ni–A (46.4) < Ni–Me (46.9) < Ni–Ph (47.2). A larger %V_{Bur} value means a wider space left for substrate coordination. The results show good agreement with Liao *et al.*[19] when increasing the bulkiness of the substituents in the α-diimine backbone structure. On the contrary, for the active complex, the trend of %V_{Bur} was Ni–A (51.7) < Ni–Ph (52.6) < Ni–Me (53.0) which shows good agreement with the experimental activities. The calculated %V_{Bur} of the active species appears to be a reliable tool for explaining several experimental data related to polymerization catalysis.[53] Our results indicated that the Ni–Me catalyst displayed the greatest performance after the activation process. The active complex of Ni–Me is covered with an alkyl group over Ni–Ph and Ni–A, respectively (Δ%V_{Bur}: Ni–Me (6.1) > Ni–Ph (5.4) > Ni–A (5.3)). Therefore, we selected Ni–Me as a starting structure to investigate the stability of the pre-catalyst complex and reaction mechanism.

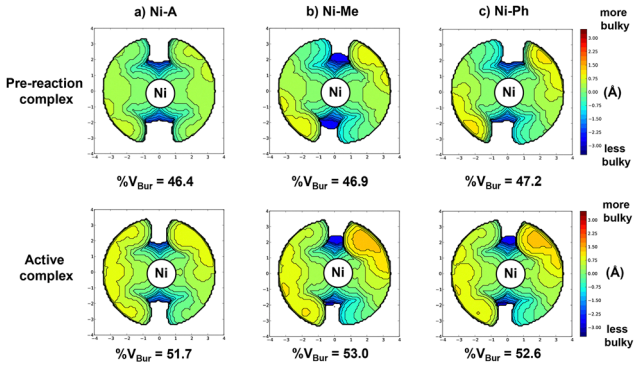

Fig. 3 Topographic steric maps of (a) Ni–A, (b) Ni–Me, and (c) Ni–Ph of the pre-catalyst complex and active complex. Curves are given in Å, with a radius of 3.5 Å.

Pre-catalyst complex

The X-ray structure of the Ni–Me catalyst was reported by Liao *et al.*[19] and its pre-catalyst complex structure adopts tetrahedral geometry. Vitek *et al.*[54] reported that singlet–triplet crossing is common in Ni–α-diimine catalysts, where transitions between low-spin square-planar and high-spin tetrahedral geometries occur naturally during the catalytic cycle. Typically, the Ni complex maintains a triplet state for its ground state, but it forces the metal center into a singlet state after monomer addition.[55]

Fig. 4 illustrates the comparison of the structures and stabilities of the complexes, highlighting the pre-catalyst complex, active complex, and π-complex reactant of the Ni–α-diimine catalyst in both singlet and triplet states. The pre-catalyst complex adopts a square-planar geometry in the singlet state and a tetrahedral geometry in the triplet state. Consequently, reactions occurring in the triplet state are based on the tetrahedral structure, while those in the singlet state rely on the square-planar structure. The active complex in the triplet state

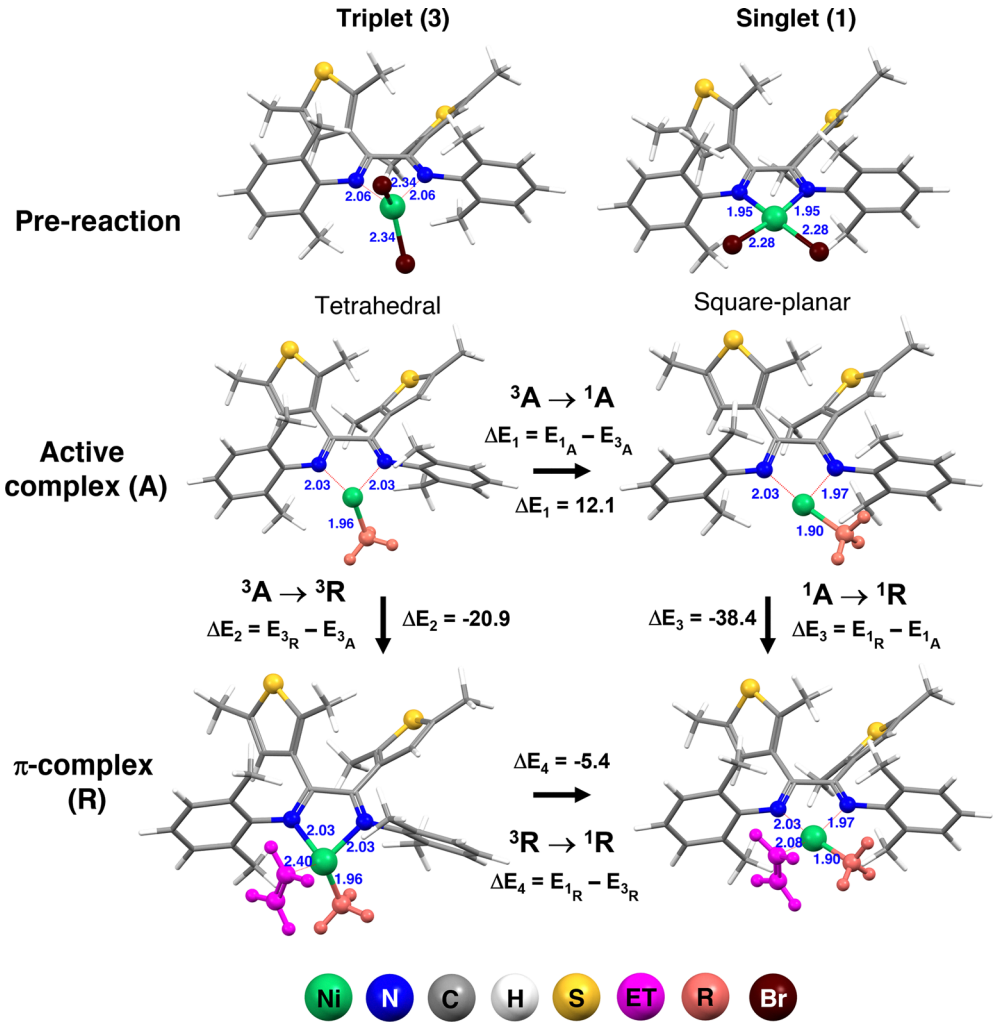

Fig. 4 The pre-catalyst complex, active complex, and π-complex in the singlet and the triplet states. The energy for each state is given in kcal mol^{-1}.

is 12.1 kcal mol^{-1} more stable than its singlet state counterpart. The transition from the active complex to the π-complex is endothermic, with energy changes of −20.9 kcal mol^{-1} in the triplet state and −38.4 kcal mol^{-1} in the singlet state. However, the π-complex reactant in the singlet state is 5.4 kcal mol^{-1} more stable than in the triplet state. Our results indicated that π-complexation between Ni–α-diimine complex and ethylene monomer is the strongest while it possesses a square-planar geometry, corresponding to Vitek *et al.*[54] Thus, we continue using this square-planar geometry as a starting structure to elucidate the reaction pathway for Ni–α-diimine catalyst in the next part.

Reaction pathway of Ni–α-diimine catalyst

Building on previous studies,[56,57] we explored the reaction mechanism of ET polymerization using Ni–α-diimine. The proposed reaction pathway, illustrated in Scheme 1, forms the basis of our investigation. Optimized structures of intermediates and transition states for ET polymerization catalyzed by Ni–α-diimine are provided in Fig. S2 of the ESI.† The relative Gibbs free energy profile for the process is depicted in Fig. 5. For the first ET insertion, from R_1 to P_1, $\Delta G_1^{\ddagger}$ is 14.2 kcal mol^{-1} while ΔG_{r1} is −15.7 kcal mol^{-1}. For the second ET insertion, from R_2 to P_2, $\Delta G_2^{\ddagger}$ and ΔG_{r2} are 10.4 kcal mol^{-1} and −20.7 kcal mol^{-1}, respectively. For the third ET insertion, from R_3 to P_3, $\Delta G_3^{\ddagger}$ is 9.7 kcal mol^{-1} and ΔG_{r3} is −19.6 kcal mol^{-1}. The observed trend is $\Delta G_3^{\ddagger} < \Delta G_2^{\ddagger} < \Delta G_1^{\ddagger}$, and $\Delta G_{r1} < \Delta G_{r3} < \Delta G_{r2}$. The first ET insertion exhibits the largest magnitude of $\Delta G_x^{\ddagger}$ compared to the second and third insertions. These results suggest that the interactions between the complex and ET monomer are strongest during the first ET insertion, making it the rate-determining (RD) step, consistent with our previous finding.[56]

Effect of metal substitutions

Several transition metal-based catalysts for ET polymerization have been developed to produce PE with higher catalytic activities and enhanced thermal stability.[58–60] In the previous section, the Gibbs free energies profile of Ni–α-diimine was investigated, and the first ET insertion was identified as the rate-determining step of the reaction. From the relative Gibbs free energies profile for ET polymerization catalyzed by Ni–α-diimine determined in the toluene solvent (Fig. S3 of the ESI†),

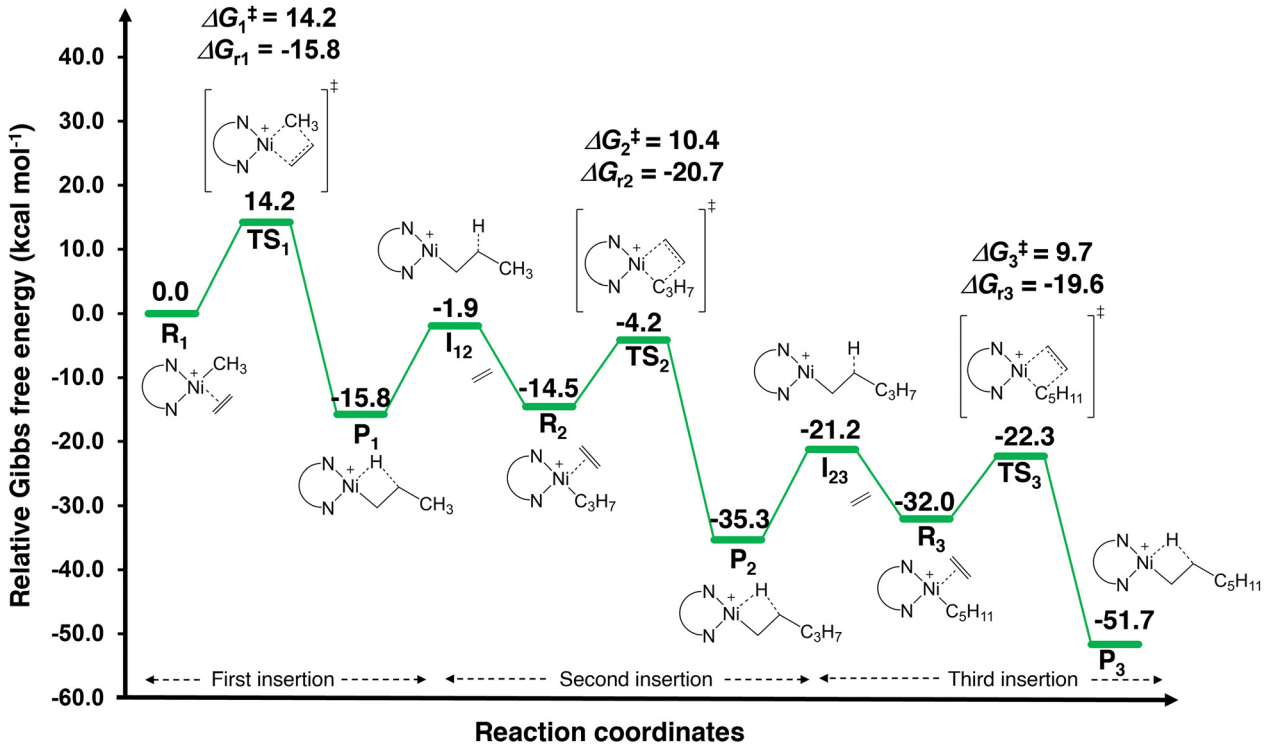

Fig. 5 The relative Gibbs free energies profile for ET polymerization catalyzed by Ni–α-diimine at 6-31G(d) levels in gas phase. The activation free energy ($\Delta G_x^{\ddagger}$), and reaction energy (ΔG_r) were shown in kcal mol^{-1}.

values of G_{cx}, $\Delta G_x^{\ddagger}$, and ΔG_{rx} show minimal variances compared to those obtained in toluene solvent. Based on the comparison of Gibbs free energy differences (G_{c1} and $\Delta G_1^{\ddagger}$) between the gas phase and toluene (as shown in Table S3 of the ESI†), solvation was found to mildly stabilize both the coordination and transition states by approximately 1–2 kcal mol^{-1}. Therefore, to reduce computational costs, all subsequent calculations were carried out in the gas phase.

In this section, the effect of metal substitutions using M–α-diimine catalysts was investigated by monitoring the reaction profiles of the RD step of ET polymerization catalyzed by M–α-diimine. Fig. S4–S13 of the ESI† provides all the optimized intermediates and transition state structures for ET polymerization catalyzed by M–α-diimine. From the structure A_1 to P_1, the G_{c1} of M–α-diimine catalysts are −13.8, −6.2, −31.0, −16.4, −2.6, 1.4, −13.0, −14.3, −18.4, 4.1, and 1.7 kcal mol^{-1}, the $\Delta G_1^{\ddagger}$ values are 12.4, 5.0, 14.3, 14.2, 14.4, 37.5, 14.7, 11.1, 9.5, 15.0, and 45.8 kcal mol^{-1}, the ΔG_{r1} values are −11.5, −15.2, −13.4, −15.7, −16.8, −16.9, −11.2, −11.6, −15.0, −17.6, and −17.3 kcal mol^{-1} for M = Mn(II), Fe(II), Co(II), Ni(II), Cu(II), Zn(II), Ru(II), Rh(II), Pd(II), Ag(I), and Cd(II), respectively. The comparison of Gibbs free energies for coordination (G_{c1}), activation Gibbs free energies ($\Delta G_1^{\ddagger}$), and reaction Gibbs free energies (ΔG_{r1}) are given in Table S4 of the ESI.†

We found that M–α-diimine catalysts with M = Mn(II), Fe(II), Ru(II), Rh(II), and Pd(II) exhibit β-agostic interactions similar to those observed in the parent Ni(II)–α-diimine system. In these complexes, the C_β–H bond distances are in the range from 1.16 to 1.17 Å, significantly elongated compared to a typical non-agostic C_β–H bond length of approximately 1.09 Å. This elongation indicates strong β-agostic interactions. In contrast, catalysts featuring M = Co(II), Cu(II), Zn(II), Ag(I), and Cd(II) do not exhibit β-agostic interactions, as evidenced by the absence of such bond elongation. This finding suggests that for metals such as Mn(II), Fe(II), Ru(II), Rh(II), and Pd(II), chain migration along the alkyl group occurs *via* a β-hydride elimination followed by re-insertion mechanism.[8,61]

Although coordination and activation free energy trends of 11 M–α-diimine catalysts (M = Mn(II), Fe(II), Co(II), Ni(II), Cu(II), Zn(II), Ru(II), Rh(II), Pd(II), Ag(I), and Cd(II)) are dissimilar, the Ag(I) complex has the weakest coordination free energy[62] while the Cd(II) complex having the highest activation free energy. Ni–α-diimine's activation and coordination free energies lie in the middle of the series. We could anticipate the difference in the catalytic performance of these catalysts to be attributed to both coordination and activation energies.[63] The coordination energy designates the binding of the monomer to the metal center, facilitating the active complex (A_1) + ethylene formation, while the activation energy reflects the stability of the transition-state (TS_1) complex.[64,65] There is no direct correlation between coordination (G_{c1}) and activation ($\Delta G_1^{\ddagger}$) free energies of M–α-diimine as portrayed in Fig. 6. In addition, the comparison of the activation free energy ($\Delta G_1^{\ddagger}$) of Pd(II) α-diimine with dibenzobarrelene derivatized with axial isopropyl groups and Ni(II), Pd(II) with thiophene backbone, is represented in Table S5 of the ESI.† The Pd(II)–α-diimine with dibenzobarrelene derivatized with axial isopropyl groups displays higher activation free energy ($\Delta G_1^{\ddagger}$ = 18.1 kcal mol^{-1}) than

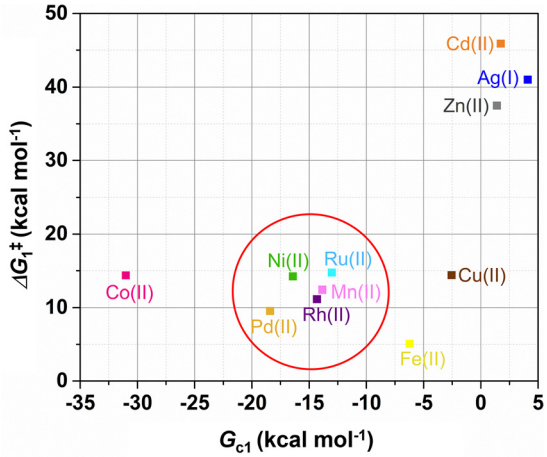

Fig. 6 The relationship between the coordination free energy (G_{c1}) and activation free energy ($\Delta G_1^{\ddagger}$) of M–α-diimine catalysts with different metal substitutions.

Ni(II) (14.2 kcal mol^{-1}) and Pd(II) (9.5 kcal mol^{-1}) with thiophene backbone. The results show good agreement with the experimental activities reported by Liao *et al.*[19] and Du *et al.*[66]

From Fig. 6, M–α-diimine catalysts are categorized into 3 clusters; Co(II) cluster, Ni(II) cluster (red circle) composed of Ni(II), Ru(II), Mn(II), Rh(II), and Pd(II), Zn(II) cluster composed of Zn(II), Cd(II), Ag(I), Cu(II). The Ni(II) cluster is of our interest, since their value G_{c1} between −20 and −10 kcal mol^{-1} and $\Delta G_1^{\ddagger}$ between 10 and 15 kcal mol^{-1}. Co(II)–α-diimine has too strong binding (<−30 kcal mol^{-1}), while those of Zn(II) cluster have too weak binding (>−5 kcal mol^{-1}). Nevertheless, an interplay between the coordination and activation free energy would determine the activity of ET polymerization catalyzed by M–α-diimine catalysts. Thus, potent M–α-diimine catalysts should bind strongly to monomers while retaining a small reaction barrier. For heterogeneous and enzymatic catalysts, the catalytic process involves the binding of the substrate to the catalyst followed by the catalytic activation, which can be described by the intrinsic activation energy (E_a(Int)). Combining G_{c1} and $\Delta G_1^{\ddagger}$, E_a(Int) of 11 M–α-diimine was computed and plotted in Fig. 7.

From Fig. 7, the Ni(II) cluster metals have (E_a(Int)) between 1.7 (Ru(II)) to −8.9 (Pd(II)) kcal mol^{-1}. The catalyst with these metals has moderate G_{c1} while having considerable low activation barrier. Among 11 M–α-diimine catalysts, only Ni–α-diimine has an experimental activity for ET polymerization.[19] From Fig. 6 and 7, Mn(II), Fe(II), Co(II), Ru(II), Rh(II), and Pd(II) emerged as strong candidates for M–α-diimine catalysts. In addition, we sought a possibility of using group III$_B$ metals for M and performed calculations on Sc(III)–α-diimine complex. The Sc(III)–α-diimine complex adopts tetrahedral geometry. It's G_{c1} and $\Delta G_1^{\ddagger}$ are −16.2 and 11.6 kcal mol^{-1}, respectively. However, the Lewis basicity of the polar co-monomers poses significant limits to electrophilic early transition metal (groups 3 and 4)-catalyzed procedures. We have now included this limitation and outlined the rationale and potential directions for future investigation of early transition metal-based catalysts.

Design of potent M–α-diimine catalysts for ethylene polymerization

To enable the design of potent M–α-diimine catalysts for ET polymerization, we searched for physical properties which can describe G_{c1} and $\Delta G_1^{\ddagger}$. Thus, the relation with steric (structural) and electronic properties of the active complex (A_1) and the transition-state complex (TS_1) of M–α-diimine catalyst for ET polymerization was investigated. The molecular electrostatic potential (MEP) maps and NBO charges of the active complexes (A_1) and transition-state (TS_1) complexes for all metal-substituted a-diimine were elucidated as shown in Fig. S14 and S15 of the ESI.† However, no correlation was found between these charge properties and G_{c1}, and $\Delta G_1^{\ddagger}$. Furthermore, the topographic steric maps of the active complexes (A_1) and transition-state complexes (TS_1) for all metal-substituted α-diimine were shown in Fig. S16 and S17 of the ESI.† On the topographic steric maps, the red color indicates the electron-rich or more negative charge region, whereas the blue color represents the electron-deficient or more positive charge region. For most metals, we found the blue color intensity to be dominant around the transition metals including polymerization area and the red color intensity to be dominant around thiophene of ligands for both A_1 and TS_1. The values of $\%V_{Bur}(TS_1)$ and $\%V_{Bur}(A_1)$ indicate the percentage of steric factors at the TS_1 and A_1 states, respectively.

Previously, Mn(II), Fe(II), Co(II), Ru(II), Rh(II), and Pd(II)–α-diimine emerged as strong candidates for M–α-diimine catalysts. However, The Fe(II), Co(II), and Ru(II) complexes demonstrate distinct structural characteristics favoring tetrahedral-like geometries in the A_1, R_1, TS_1, and P_1 states. Their exclusion from further analysis was based on the mismatch between their preferred geometry and the established reaction mechanism observed for parent Ni–α-diimine systems, which proceeds *via* a square-planar coordination. Thus, these three metal complexes would have been identified as distinct from the Ni(II)–diimine group. Therefore, the analysis was based on the evaluation of M–α-diimine catalysts from three metal groups (group I: Mn(II), Ni(II), Rh(II), Pd(II), group II: Fe(II), Co(II), Ru(II), and group III: Cu(II), Zn(II), Ag(I), Cd(II)). The value of G_{c1}, $\Delta G_1^{\ddagger}$, bond distances, NBO charges, and percent buried volume ($\%V_{Bur}$) were summarized in Tables S6 and S7 of the ESI.†

Scheme 2 illustrates the correlations between energy criteria (G_{c1} and $\Delta G_1^{\ddagger}$) and the steric (bond distance, $\%V_{Bur}$) and electronic (NBO charges) descriptors categorized into three M–α-diimine groups.

The metals in group I (Mn(II), Ni(II), Rh(II), and Pd(II)) can be classified as potential active catalysts, as their catalytic performance is similar to that of the parent Ni–α-diimine complex. With Pd(II), M–α-diimine shows the strongest G_{c1} value (−18.4 kcal mol^{-1}), suggesting significant catalytic potential, followed by the parent Ni(II)–α-diimine complex, which also shows good performance with a strong G_{c1} value (−16.4 kcal mol^{-1}). However, we could not find a correlation (R^2) greater than 0.7 between G_{c1} and the steric (bond distance, $\%V_{Bur}$) or electronic (NBO charges) descriptors for this group. On the other hand,

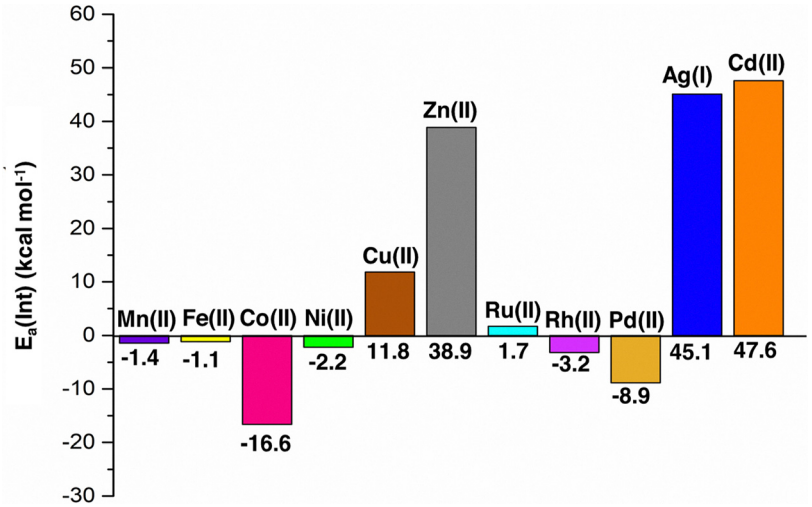

Fig. 7 The intrinsic activation energy (E_a(Int)) values of M–α-diimine catalysts with different metal substitutions.

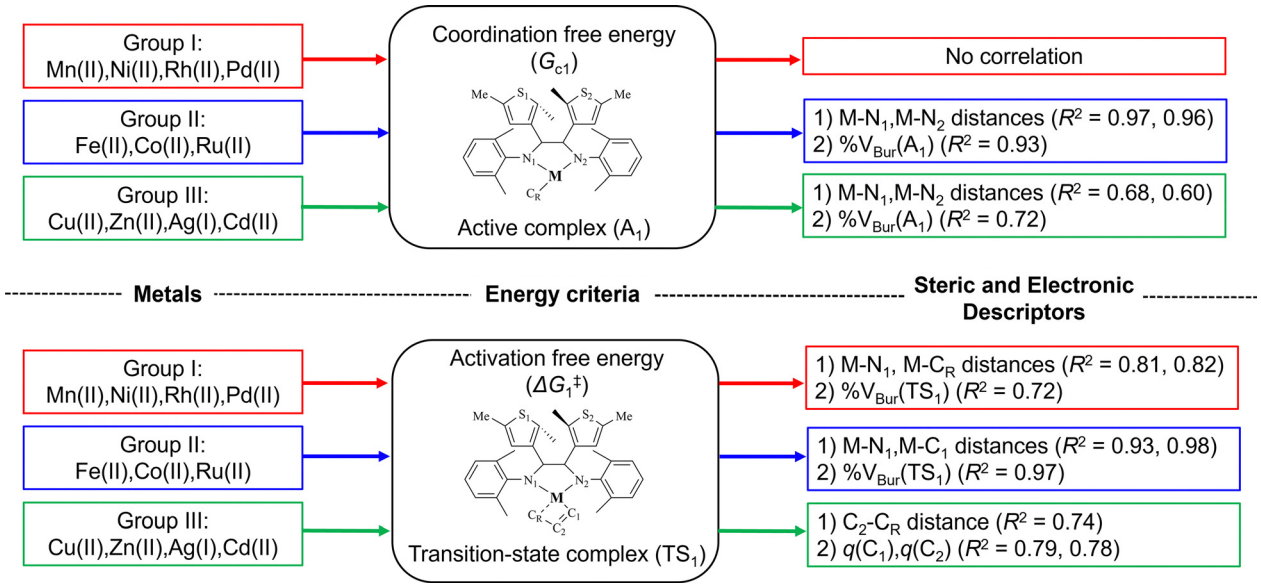

Scheme 2 The best three correlation coefficients between the energy criteria and the steric and electronic descriptors of three metal groups.

their $\Delta G_1^{\ddagger}$ values show R^2 exceeding 0.7 for M–N_1 distance, M–C_R distance, and %V_{Bur} of TS_1. We observed the increase of M–N_1 distances ranging from 1.93 to 2.08 Å and M–C_R distances from 2.00 to 2.21 Å with the decrease in $\Delta G_1^{\ddagger}$ values. This indicates that the catalyst with a tighter bonding between metal and ligand/propagating chain has lower activation and enhances the activity. Additionally, the decrease of %V_{Bur}(TS_1) ranging from 50.4 to 46.5% coincides with the lowering of $\Delta G_1^{\ddagger}$ values. This suggests the reaction barrier to be align with the steric surrounding the active center. The tightening of metal and ligand/propagating chain reduces the steric interaction surrounding the active center.

Group II metals (Fe(II), Co(II), and Ru(II)) exhibit varied behaviors. Despite showing a relatively weak G_{c1} value (−6.2 kcal mol^{-1}), Fe(II) has a significantly lower $\Delta G_1^{\ddagger}$ value (5.08 kcal mol^{-1}) compared to the parent Ni(II)–α-diimine complex (14.2 kcal mol^{-1}), suggesting a high kinetic favorability. Co(II) has the strongest G_{c1} (−31.0 kcal mol^{-1}) and a high $\Delta G_1^{\ddagger}$ (14.37 kcal mol^{-1}). Ru(II) shows intermediate values for both G_{c1} (−13.0 kcal mol^{-1}) and $\Delta G_1^{\ddagger}$ (14.7 kcal mol^{-1}). We found two descriptors which have strong correlation (R^2 > 0.7) with G_{c1}, M–N_1 distance, and %V_{Bur} of A_1 complex. Again, no charge properties were noticed to have a high correlation with G_{c1} values. The trends of M–N_1 distance and G_{c1} are Fe (1.89 Å) > Ru (1.94 Å) > Co (2.01 Å) and Fe (−6.2 kcal mol^{-1}) < Ru (−13.0 kcal mol^{-1}) < Co (−31.0 kcal mol^{-1}), respectively. Additionally, the decline of %V_{Bur}(A_1) (Fe(II) > Ru(II) > Co(II)) corresponds to the gain of coordination free energy. This implies that while raising the steric hindrance, the increase of M–N_1 bond strength stipulates a weaker coordination of

ethylene with metal. Similarly, the descriptor which has high correlation with $\Delta G_1^{\ddagger}$ values is M–C_R distance of the transition state complex. For this group, we were aware that it contains only three data points where statistics does not always make sense. Thus, three parameters, M–N_1 and M–C_1 distances and $\%V_{Bur}(TS_1)$, though have high R^2 values, were excluded from further analysis. For group II, $\Delta G_1^{\ddagger}$ value increases with the increment of M–C_R distance. Thus, the strong bond with the propagating chain reduces the activation barrier (Fe (5.1 kcal mol^{-1}) < Co (14.4 kcal mol^{-1}) < Ru (14.7 kcal mol^{-1})). For this group, even though Ru(II) has a distinctively high activation barrier, it can be considered an active catalyst. On the other hand, Co(II) expresses non-β-agostic interactions and, thus, could be disqualified from the list of potential active catalysts.

Group III metals (Cu(II), Zn(II), Ag(I), and Cd(II)) do not have good performance. These metals exhibit weak G_{c1} values (−2.6 to 4.1 kcal mol^{-1}) and high $\Delta G_1^{\ddagger}$ values, for example; Cd(II) shows $\Delta G_1^{\ddagger}$ of 45.9 kcal mol^{-1}. For G_{c1} values, only $\%V_{Bur}(A_1)$ shows R^2 greater than 0.7 with the following trends: $\%V_{Bur}(A_1)$: G_{c1} Cu(II) (50.7%: −2.6 kcal mol^{-1}) > Zn(II) (49.5%: 1.4 kcal mol^{-1}) > Cd(II) (43.3%: 1.7 kcal mol^{-1}) ∼ Ag(I) (40.0%: 4.1 kcal mol^{-1}). The coordination of ethylene loosened when the active center becomes less steric. This corresponds to the longer M–N distances compared with other groups. Thus, the metals of this group are less tightly bound with the ligand. The more steric would represent a strong metal interaction. For $\Delta G_1^{\ddagger}$ values, we saw three NBO charge descriptors (C_1, C_2, and C_R) and one geometrical parameter, C_2–C_R distance of the TS_1 complex showing high correlation. The more negative C_1 and C_R charges, the less negative C_2, and the elongated C_2–C_R distances trigger the lower activation. From these trends, we could assume that the monomer and growing chain interactions stabilized the transition state complex and are the key factor for the activity of catalysts from this group of metals. However, the steric and electronic descriptors indicated weak interactions between the metal center and the α-diimine ligand. Thus, the metals in group III can be classified as inactive catalysts.

Overall, Mn(II), Rh(II), Pd(II), Fe(II), and Ru(II) emerged as the most promising catalytic candidates.

Despite our computational model identifying Mn(II), Rh(II), Pd(II), Fe(II), and Ru(II) α-diimine complexes as promising candidates based on energy criteria (G_{c1}, $\Delta G_1^{\ddagger}$), we acknowledge a key discrepancy. Ni(II) and Pd(II) remain the experimentally validated benchmarks for ethylene polymerization, consistently demonstrating high activity and robust performance across a range of conditions.[20–26] This inconsistency between theory and experiment highlights the need for a deeper examination of the underlying theoretical assumptions and performance metrics. While Mn(II), Rh(II), Pd(II), Fe(II), and Ru(II) demonstrate computational promise, there is currently limited experimental evidence supporting their high catalytic activity. These findings emphasize the importance of combining theoretical descriptors with established empirical performance metrics, particularly when ranking catalyst candidates. The dominant position of Ni(II) and Pd(II) in the literature and industry reinforces their role as the gold standard for α-diimine-based olefin polymerization catalysts.[22,25,26]

Conclusions

In this study, we employed DFT calculations to investigate the reaction mechanism of Ni–α-diimine catalysts in ethylene (ET) polymerization, focusing on structural and electronic factors affecting activity. Ni–Me, the most active catalyst, serves as a benchmark for stability and mechanism analysis. Among pre-catalyst complexes, the tetrahedral geometry is most stable and matches X-ray data, while the square-planar geometry of the reactant π-complex is better suited for reaction mechanism studies.

The first ET insertion is the rate-determining step, showing the highest coordination energies (G_{c1}) and activation free energies ($\Delta G_1^{\ddagger}$). Comparing M–α-diimine complexes with various transition metals revealed three clusters based on G_{c1} and $\Delta G_1^{\ddagger}$. The most promising cluster Ni(II), Mn(II), Ru(II), Rh(II), and Pd(II) displays moderate metal–ligand binding (G_{c1} between −20 and −10 kcal mol^{-1}) and reasonable activation barriers ($\Delta G_1^{\ddagger}$ between 10 and 15 kcal mol^{-1}), balancing stability and reactivity.

Correlation of electronic descriptors (*e.g.*, electrostatic potentials, NBO charges) with catalytic performance were inconclusive. In contrast, steric parameters such as M–N_1 and M–C_R bond lengths, along with percent buried volume ($\%V_{Bur}$), showed stronger correlations with activation free energy. The catalysts were classified into three groups: group I (Mn(II), Ni(II), Rh(II), Pd(II)) exhibited the highest catalytic potential, with Pd(II) displaying the most favorable G_{c1} values and steric correlations; group II (Fe(II), Co(II), Ru(II)) demonstrated structural diversity and variable activity—Ru(II) remained viable despite a slightly higher activation barrier than the parent Ni(II), while Co(II) was less effective due to the absence of β-agostic interactions; group III (Cu(II), Zn(II), Ag(I), Cd(II)) showed poor performance, attributed to weak substrate binding and high activation barriers.

Overall, Mn(II), Rh(II), Pd(II), Fe(II), and Ru(II) emerged as promising candidates based on computational studies. However, to date, only Ni(II) and Pd(II) have been experimentally validated, revealing a gap between theoretical predictions and practical realization. These results emphasize the critical need to integrate computational modeling with experimental validation to effectively guide the rational design of next-generation ethylene polymerization catalysts.

Author contributions

Pavee Apilardmongkol: calculations, methodology, conceptualization, visualization, writing – original draft manuscript. Manussada Ratanasak: conceptualization, validation, writing – review and editing. Tatiya Chokbunpiam: visualization, conceptualization, writing – review and editing. Fadjar Mulya: calculations, validation. Wilasinee Santiwarodom: visualization, calculations. Thanawit Kuamit: calculations, validation. Yasuteru Shigeta: supervision, writing – review and editing. Junya Hasegawa: supervision, writing – review and editing. Vudhichai Parasuk: software, conceptualization, supervision, writing – review and editing.

Conflicts of interest

There are no conflicts to declare.

Data availability

The data that support the findings of this study are available from the corresponding author upon reasonable request.

Acknowledgements

This research is supported by Ratchadapisek Somphot Fund for Postdoctoral Fellowship, Chulalongkorn University. We are gratefully thankful to the Center of Excellence in Computational Chemistry (CECC), NSTDA Supercomputer center (ThaiSC) for providing high performance computing services and facilities. A part of the research was supported by MEXT Promotion of Development of a Joint Usage/Research System Project: Coalition of Universities for Research Excellence Program (CURE): Grant Number JPMXP1323015474. A part of computations was performed at the Research Center for Computational Science (RCCS), Okazaki, Japan (Project: 24-IMS-C103, 25-IMS-C103). J. H. acknowledged the Photoexcitonix Project at Hokkaido University.

References

1 W. Kaminsky, *Macromol. Chem. Phys.*, 2008, **209**, 459–466.
2 K. Soga and T. Shiono, *Prog. Polym. Sci.*, 1997, **22**, 1503–1546.
3 Q. Li, C. Wang, H. Mu and Z. Jian, *J. Catal.*, 2021, **400**, 332–337.
4 A. Zhou, R. Yuan, Q. Mahmood, S. Yuan, Y. Wang, Z. Hu, S. Zou, T. Liang and W.-H. Sun, *Polym. Chem.*, 2024, **15**, 4029–4043.
5 Y. Liao, Y. Zhang, L. Cui, H. Mu and Z. Jian, *Organometallics*, 2019, **38**, 2075–2083.
6 G. Ren, R. Yuan, Q. Mahmood, Y. Zeng, Y. Wang, Z. Hu, S. Zou, T. Liang and W.-H. Sun, *J. Mol. Struct.*, 2024, **1316**, 139037.
7 Z. Chen and M. Brookhart, *Acc. Chem. Res.*, 2018, **51**, 1831–1839.
8 M. D. Leatherman, S. A. Svejda, L. K. Johnson and M. Brookhart, *J. Am. Chem. Soc.*, 2003, **125**, 3068–3081.
9 S. D. Ittel, L. K. Johnson and M. Brookhart, *Chem. Rev.*, 2000, **100**, 1169–1204.
10 J. Zhang, X. Wang and G.-X. Jin, *Coord. Chem. Rev.*, 2006, **250**, 95–109.
11 L. Guo, W. Liu and C. Chen, *Mater. Chem. Front.*, 2017, **1**, 2487–2494.
12 D. P. Gates, S. A. Svejda, E. Oñate, C. M. Killian, L. K. Johnson, P. S. White and M. Brookhart, *Macromolecules*, 2000, **33**, 2320–2334.
13 C. Wang, D. Wang, Z. Fu, Y. Qin, Q. Zhang and Z. Fan, *J. Catal.*, 2022, **413**, 311–320.
14 L. Zhu, D. Zang, Y. Wang, Y. Guo, B. Jiang, F. He, Z. Fu, Z. Fan, M. A. Hickner, Z.-K. Liu and L.-Q. Chen, *Organometallics*, 2017, **36**, 1196–1203.
15 F. Wang and C. Chen, *Polym. Chem.*, 2019, **10**, 2354–2369.
16 K. Song, W. Yang, B. Li, Q. Liu, C. Redshaw, Y. Li and W.-H. Sun, *Dalton Trans.*, 2013, **42**, 9166–9175.
17 L. Zhong, G. Li, G. Liang, H. Gao and Q. Wu, *Macromolecules*, 2017, **50**, 2675–2682.
18 H. Wang, W. Lu, M. Zou and S. Dai, *Molecules*, 2023, **28**, 2266.
19 D. Liao, S. Behzadi, C. Hong, C. Zou, M. Qasim and M. Chen, *Appl. Organomet. Chem.*, 2021, **35**, e6406.
20 K. E. Allen, J. Campos, O. Daugulis and M. Brookhart, *ACS Catal.*, 2015, **5**, 456–464.
21 Y. Zhang, C. Wang, S. Mecking and Z. Jian, *Angew. Chem., Int. Ed.*, 2020, **59**, 14296–14302.
22 H. Fan, X. Kang and S. Dai, *ACS Catal.*, 2024, **14**, 13531–13541.
23 M. Ma and S. Dai, *Polymer*, 2024, **307**, 127292.
24 Z. Lu, X. Xu, Y. Luo, S. He, W. Fan and S. Dai, *ACS Catal.*, 2023, **13**, 725–734.
25 B. Ding, L. Jiang, X. Kang and S. Dai, *Chin. J. Chem.*, 2023, **41**, 1509–1516.
26 Z. Lu, Y. Ge and S. Dai, *Inorg. Chem.*, 2023, **62**, 14888–14895.
27 H. Zheng, Y. Li, W. Du, C. S. Cheung, D. Li, H. Gao, H. Deng and H. Gao, *Macromolecules*, 2022, **55**, 3533–3540.
28 M. Yan, X. Kang, S. Li, X. Xu, Y. Luo, S. He and C. Chen, *Organometallics*, 2022, **41**, 3212–3218.
29 E. J. Arlman and P. Cossee, *J. Catal.*, 1964, **3**, 99–104.
30 M. Brookhart, M. L. H. Green and G. Parkin, *Proc. Natl. Acad. Sci. U. S. A.*, 2007, **104**, 6908–6914.
31 D. Zhang, E. T. Nadres, M. Brookhart and O. Daugulis, *Organometallics*, 2013, **32**, 5136–5143.
32 H. Saeed, Q. Mahmood, Y. Ma, K. F. Tahir, G. Ren, Y. Wang and W.-H. Sun, *ChemCatChem*, 2025, **17**, e202401640.
33 Q. Mahmood, Z. Hu, G. Ren and W.-H. Sun, *Coord. Chem. Rev.*, 2025, **541**, 216833.
34 T. Yoshida, N. Koga and K. Morokuma, *Organometallics*, 1995, **14**, 746–758.
35 L. Deng, P. Margl and T. Ziegler, *J. Am. Chem. Soc.*, 1997, **119**, 1094–1100.
36 Z. Song, R. Gao, C. Wu, Q. Gou, G. Zheng, J. Liu, S. Yang and H. Feng, *Polymers*, 2024, **16**, 762.
37 I. E. Soshnikov, N. V. Semikolenova, K. P. Bryliakov and E. P. Talsi, *Catalysts*, 2021, **11**, 1386.
38 H. Liu, Y. Liu, J. Jiang and Z. Ke, *Eur. Polym. J.*, 2025, **222**, 113587.
39 J. Chen, Y. Gao and T. J. Marks, *Angew. Chem., Int. Ed.*, 2020, **59**, 14726–14735.
40 M. J. Frisch, G. W. Trucks, H. B. Schlegel, G. E. Scuseria, M. A. Robb, J. R. Cheeseman, G. Scalmani, V. Barone, G. A. Petersson, H. Nakatsuji, X. Li, M. Caricato, A. V. Marenich, J. Bloino, B. G. Janesko, R. Gomperts, B. Mennucci, H. P. Hratchian, J. V. Ortiz, A. F. Izmaylov, J. L. Sonnenberg, D. Williams-Young, F. Ding, F. Lipparini, F. Egidi, J. Goings, B. Peng, A. Petrone, T. Henderson,

D. Ranasinghe, V. G. Zakrzewski, J. Gao, N. Rega, G. Zheng, W. Liang, M. Hada, M. Ehara, K. Toyota, R. Fukuda, J. Hasegawa, M. Ishida, T. Nakajima, Y. Honda, O. Kitao, H. Nakai, T. Vreven, K. Throssell, J. A. Montgomery, Jr., J. E. Peralta, F. Ogliaro, M. J. Bearpark, J. J. Heyd, E. N. Brothers, K. N. Kudin, V. N. Staroverov, T. A. Keith, R. Kobayashi, J. Normand, K. Raghavachari, A. P. Rendell, J. C. Burant, S. S. Iyengar, J. Tomasi, M. Cossi, J. M. Millam, M. Klene, C. Adamo, R. Cammi, J. W. Ochterski, R. L. Martin, K. Morokuma, O. Farkas, J. B. Foresman and D. J. Fox, *Gaussian 16, Rev. C.01*, Gaussian Inc., Wallingford, CT, 2016.

41 J.-D. Chai and M. Head-Gordon, *Phys. Chem. Chem. Phys.*, 2008, **10**, 6615–6620.

42 S. Grimme, *Wiley Interdiscip. Rev.: Comput. Mol. Sci.*, 2011, **1**, 211–228.

43 K. E. Riley, K.-A. Tran, P. Lane, J. S. Murray and P. Politzer, *J. Comput. Sci.*, 2016, **17**, 273–284.

44 W. G. Xu and B. Jin, *Chem. Phys. Lett.*, 2006, **419**, 439–443.

45 A. Posada-Borbón and A. Posada-Amarillas, *Chem. Phys. Lett.*, 2015, **618**, 66–71.

46 A. E. Reed and F. Weinhold, *J. Chem. Phys.*, 1983, **78**, 4066–4073.

47 A. E. Reed, R. B. Weinstock and F. Weinhold, *J. Chem. Phys.*, 1985, **83**, 735–746.

48 F.-S. Liu, H.-B. Hu, Y. Xu, L.-H. Guo, S.-B. Zai, K.-M. Song, H.-Y. Gao, L. Zhang, F.-M. Zhu and Q. Wu, *Macromolecules*, 2009, **42**, 7789–7796.

49 S. Ahmadjo, S. Damavandi, G. H. Zohuri, A. Farhadipour and Z. Etemadinia, *J. Organomet. Chem.*, 2017, **835**, 43–51.

50 L. Zhong, C. Du, G. Liao, H. Liao, H. Zheng, Q. Wu and H. Gao, *J. Catal.*, 2019, **375**, 113–123.

51 L. Falivene, Z. Cao, A. Petta, L. Serra, A. Poater, R. Oliva, V. Scarano and L. Cavallo, *Nat. Chem.*, 2019, **11**, 872–879.

52 A. Poater, F. Ragone, S. Giudice, C. Costabile, R. Dorta, S. P. Nolan and L. Cavallo, *Organometallics*, 2008, **27**, 2679–2681.

53 L. Falivene, L. Cavallo and G. Talarico, *ACS Catal.*, 2015, **5**, 6815–6822.

54 A. K. Vitek, A. K. Leone, A. J. McNeil and P. M. Zimmerman, *ACS Catal.*, 2018, **8**, 3655–3666.

55 R. C. Chapleski, J. L. Kern, W. C. Anderson, B. K. Long and S. Roy, *Catal. Sci. Technol.*, 2020, **10**, 2029–2039.

56 P. Apilardmongkol, M. Ratanasak, J. Hasegawa and V. Parasuk, *ChemCatChem*, 2022, **14**, e202200028.

57 P. Apilardmongkol, M. Ratanasak, J. Hasegawa and V. Parasuk, *J. Mol. Graphics Modell.*, 2023, **125**, 108586.

58 D. H. Camacho and Z. Guan, *Chem. Commun.*, 2010, **46**, 7879–7893.

59 Y. Wang, R. Gao, Q. Gou, J. Lai, R. Zhang, X. Li and Z. Guo, *Eur. Polym. J.*, 2022, **181**, 111693.

60 W. Ullah Khan, H. Mazhar, F. Shehzad and M. A. Al-Harthi, *Chem. Rec.*, 2023, **23**, e202200243.

61 Z. Ye, J. Jiang, C. Zhao and Z. Ke, *Macromolecules*, 2024, **57**, 11461–11475.

62 B. T. Watson, M. Vanga, A. Noonikara-Poyil, A. Muñoz-Castro and H. V. R. Dias, *Inorg. Chem.*, 2023, **62**, 1636–1648.

63 L. Zhu, S. Li, X. Kang, W. Zhang and Y. Luo, *Catalysts*, 2023, **13**, 1026.

64 K. Nomura, W. Wang, M. Fujiki and J. Liu, *Chem. Commun.*, 2006, 2659–2661, DOI: **10.1039/B605005K**.

65 S. Vyazovkin, *Polymers*, 2020, **12**, 1070.

66 C. Du, L. Zhong, J. Gao, S. Zhong, H. Liao, H. Gao and Q. Wu, *Polym. Chem.*, 2019, **10**, 2029–2038.